Article

Effect of Ni Substitution on Thermoelectric Properties of Bulk β-Fe$_{1-x}$Ni$_x$Si$_2$ (0 ≤ x ≤ 0.03)

Sopheap Sam, Soma Odagawa, Hiroshi Nakatsugawa and Yoichi Okamoto

Special Issue

Materials Physics in Thermoelectric Materials

Edited by
Prof. Dr. Bao-Tian Wang and Dr. Peng-Fei Liu

Article

Effect of Ni Substitution on Thermoelectric Properties of Bulk β-Fe$_{1-x}$Ni$_x$Si$_2$ (0 ≤ x ≤ 0.03)

Sopheap Sam [1], Soma Odagawa [1], Hiroshi Nakatsugawa [1,*] and Yoichi Okamoto [2]

[1] Yokohama National University, Yokohama 240-8501, Japan
[2] National Defense Academy, Yokosuka 239-8686, Japan
* Correspondence: nakatsugawa-hiroshi-dx@ynu.ac.jp

Abstract: A thermoelectric generator, as a solid-state device, is considered a potential candidate for recovering waste heat directly as electrical energy without any moving parts. However, thermoelectric materials limit the application of thermoelectric devices due to their high costs. Therefore, in this work, we attempt to improve the thermoelectric properties of a low-cost material, iron silicide, by optimizing the Ni doping level. The influence of Ni substitution on the structure and electrical and thermoelectric characteristics of bulk β-Fe$_x$Ni$_{1-x}$Si$_2$ (0 ≤ x ≤ 0.03) prepared by the conventional arc-melting method is investigated. The thermoelectric properties are reported over the temperature range of 80–800 K. At high temperatures, the Seebeck coefficients of Ni-substituted materials are higher and more uniform than that of the pristine material as a result of the reduced bipolar effect. The electrical resistivity decreases with increasing x owing to the increases in metallic ε-phase and carrier density. The ε-phase increases with Ni substitution, and solid solution limits of Ni in β-FeSi$_2$ can be lower than 1%. The highest power factor of 200 μWm^{-1}K^{-2} at 600 K is obtained for x = 0.001, resulting in the enhanced *ZT* value of 0.019 at 600 K.

Keywords: iron silicide; bipolar effect; Ni doping; thermoelectric properties; *ZT* values

1. Introduction

Thermoelectricity has been considered a potential technique to recover waste heat into electrical energy through the Seebeck effect without exhaust gas pollution to the environment, with no moving parts, and with no necessary maintenance required. To achieve highly efficient thermoelectric (TE) devices, finding promising semiconducting materials is the main challenge. Traditional TE materials such as PbTe and Bi$_2$Te$_3$ are high-priced and toxic; therefore, researchers have been trying to develop abundant and non-toxic materials, such as binary copper chalcogenide [1], copper sulfide compound [2,3], iron silicide [4–8], and other materials, in order to replace those traditional ones. Iron silicide compound is an abundant and non-toxic material having three different kinds of phases, such as the cubic ε-phase with space group $P2_13$ [4,5], the tetragonal α-phase with space group $P4/mmm$ [6,7], and the orthorhombic β-phase with space group $Cmce$ [8]. According to Piton and Fay diagram [9], the semiconducting β-phase can be formed at a temperature below 1259 K and depends on the kind and amount of external impurity doping, whereas the metallic ε and α-phases are grown at a higher temperature. It is noticed that its ε and α-phases are a metal that is not suitable for TE applications due to the deterioration of the Seebeck coefficient ($S = -\Delta V/\Delta T$, where ΔV and ΔT are the TE voltage and temperature difference across the material, respectively). However, its β-phase, a semiconducting material with a small band gap of around 0.7 eV [10], is suitable in TE applications. In addition, compared to other traditional TE materials (PbTe and Bi$_2$Te$_3$), β-FeSi$_2$ can work at high temperatures due to strong oxidation resistance, good thermal stability, and low cost [11–15]. However, due to its narrow band gap and low carrier concentration (n_H) of around 10^{16} cm^{-3}, the bipolar effect usually occurs in a non-doped β-FeSi$_2$, especially in

high-temperature regions, resulting in a decline of the $|S|$. The Seebeck effect is generated by two types of carriers having opposite signs. With the increased temperature and low n_H, the total Seebeck effect is cancelled out, which is unfavorable for TE applications [16–18]. Therefore, as temperature increases, the TE performance is defined by $ZT = S^2\rho^{-1}\kappa^{-1}T$, where S, ρ, κ, and T are Seebeck coefficient, electrical resistivity, total thermal conductivity, and temperature, respectively. The Seebeck coefficient worsens due to the decrease in $|S|$ caused by the bipolar effect. The pristine β-FeSi$_2$ has a low value of ZT of only round 2×10^{-4} [19]. To solve this issue, doping with impurities having a large valence electron in either Fe or Si sites is considered an effective technique for increasing the n_H, resulting in an improvement in the stability of $|S|$ [17]. In addition, the ρ is inversely proportional to the n_H; therefore, it can be simultaneously decreased owing to the increase in n_H. As a result, the ZT can be significantly improved due to the monotonicity in $|S|$ and the decrease in ρ. Theoretically, it was reported that the optimum n_H to improve the TE performance of β-FeSi$_2$ is approximately within the range of 1×10^{20} to 2×10^{21} cm^{-3} [15]. In fact, we prepared β-Fe$_{0.97}$Co$_{0.03}$Si$_2$ with the arc melting method and found a ZT value of 0.099 at 800 K [20]. Furthermore, many previous works [21–30] attempted to enhance the n_H of β-FeSi$_2$ via doping with various impurities.

Ito et al. reported the TE characteristics of β-FeSi$_{2-x}$P$_x$ fabricated by mechanical alloyed (MA) and hot-pressed (HP) method. By doping P at the Si site, the S was negative, indicating the n-type material with the optimum concentration of x = 0.02, and the ρ slightly decreased with a considerable increase in P content due to the increase in n_H. As a result, the highest ZT of about 0.033 at 672 K was obtained with x = 0.02, which was about 11 times higher than that of the non-doped sample [21]. In addition, Tani and Kido found that the ZT of β-FeSi$_2$ can be enhanced up to 0.14 at 847 K by doping with Pt as an impurity [22]. Ohtaki et al. investigated various impurities for doping, such as Cu, Zn, Nb, Ag, Sb, and Mn, by analyzing the microstructural changes and TE performance of β-FeSi$_2$. They reported that the microstructures were remarkably changed by those impurities. The highest ZT value of about 0.026 was obtained by 3% Mn doping at 873 K [23]. In addition, Chen et al. investigated the thermoelectric characteristics of Co addition on β-FeSi$_2$ fabricated by rapid solidification and followed the HP method. It was reported that the optimum doping to achieve maximum $ZT = 0.25$ was obtained in Fe$_{0.94}$Co$_{0.06}$Si$_2$ samples due to the enhancement in S and a significant reduction in ρ [24]. Furthermore, Du et al. attempted to improve the TE performance of the previous Fe$_{0.94}$Co$_{0.06}$Si$_2$ by doping with an additional impurity element named Ru. It was found that Ru doping significantly decreases the thermal conductivity because the strain field and mass oscillation scatter the phonons, resulting in the improvement of $ZT = 0.33$ at 900 K [25]. Moreover, Dabrowski et al. investigated the effects of several dopants, namely, Mn, Co, Al, and P, on the TE properties of β-FeSi$_2$. They reported that compared to other dopants, P was not effective at improving the ZT due to only a slight decrease in ρ, where the n_H of the P-doped sample was probably lower than that of other impurity-doped samples; however, the highest ZT was obtained in a Co-doped sample, probably due to the high n_H [26]. Qiu et al. have recently reported that by doping 16% Ir into the Fe site of β-FeSi$_2$, the ZT can be greatly improved to 0.6 at 1000 K due to the significant reductions in ρ and κ, resulting from high n_H and phonon–electron scattering, respectively [27]. Based on a series of previous reports, it is worth noticing that doping with elements having large valence electrons to either Fe or Si sites of β-FeSi$_2$-based materials is remarkably effective at improving the n_H and the TE performance.

Since Ni has two valence electrons more than Fe, the n_H can be possibly increased by substituting Ni into the Fe site of β-FeSi$_2$. Komabayashi et al. reported that the S, ρ, and power factor ($PF = S^2\rho^{-1}$) at room temperature of Fe$_{0.94}$Ni$_{0.06}$Si$_{2.05}$ thin film fabricated by the RF sputtering method were -113 µVK^{-1}, 0.076 Ωcm, and 17 µWm^{-1}K^{-2}, respectively [28]. In addition, Nagai et al. investigated the effect of Ni addition on the PF of β-FeSi$_2$ fabricated by mechanical alloying and hot-pressing techniques. The highest $|S|$ was obtained after 1% Ni doping—240 µVK^{-1} at 600 K—and ρ significantly decreased

with Ni addition. This indicates that both *S* and ρ can be simultaneously improved by Ni addition, contributing to the enhancement of *PF* [29]. Furthermore, Tani and Kido reported that the ρ of bulk β-Fe$_{1-x}$Ni$_x$Si$_2$ decreased with the substitution of Ni owing to the increase in n_H [30]; thus, a reduction in the bipolar effect should be achieved. However, there are only a few reports regarding the effect of Ni doping of β-FeSi$_2$, and an investigation on the thermal conductivity (κ) and the *ZT* values has not been reported. Moreover, the optimum Ni doping concentration needed to improve the TE performance of β-Fe$_{1-x}$Ni$_x$Si$_2$ also has not been investigated yet.

In this work, we attempted to improve the electrical and thermoelectric properties of the bulk of binary β-FeSi$_2$ by Ni substitution into the Fe site prepared by the facile arc-melting techniques and directly followed by a heat treatment and annealing process. For the β-Fe$_{1-x}$Ni$_x$Si$_2$ system ($0 \leq x \leq 0.03$), a detailed investigation of the optimum doping level of Ni to enhance TE performance is reported for the temperature range of 80–800 K.

2. Materials and Methods

2.1. Sample Fabrication

The raw materials of Fe grain (99.9% up, 3Nup, High Purity Chemicals, Japan), Si grain (99.999%, 5N, High Purity Chemicals, Japan), and Ni grain (99.9%, 3N, High Purity Chemicals, Japan) were prepared following the composition of Fe$_x$Ni$_{1-x}$Si$_2$, where $0 \leq x \leq 0.03$. The melting process was performed by using the arc-melting method under a vacuum of about $2–5 \times 10^{-5}$ torr in an argon (Ar) atmosphere to prevent oxidation during melting. In addition, titanium (Ti) 10 g was set and initially melted before the main materials to remove the residual oxygen inside the melting chamber. To get an ingot with a homogeneous material distribution, it was flipped and remelted three times. The numerical control (NC) wire-cutting machine (EC-3025, Makino) was then used to slice the ingots into small pieces (sample's size W × L × T = 7 × 7 × 1.5 mm) to facilitate the characterization of TE properties. The pieces were then polished in order to remove the oxidized surface before the heat-treatment process. The metallic ε and α-phases were formed during the arc-melting process. In order to transform into the β-phase, the heat-treatment process at 1423 K for 3 h, and consequently, the annealing process at 1113 K for 20 h, were applied for all samples in vacuumed silica quartz ampule. The first step of heat treatment was to additionally homogenize the material distribution, and the second step was to transform it into a single β-phase. The heat treatment and annealing process followed that of reference [23], where the optimum condition was reported.

2.2. Sample Characterization

The CuKα high-resolution X-ray diffractometer (SmartLab, Rigaku, Tokyo, Japan) was used for the powder X-ray diffraction (XRD) measurements. With Rietveld analysis utilizing the RIETAN-FP software, calculation of the crystal structure parameters and phase identification were carried out by using the measured XRD data. A scanning electron microscope (VE-8800, KEYENCE, Osaka, Japan) apparatus was then used to observe the surface structure of each of the fabricated materials. The elemental analysis was performed with a scanning electron microscope (SU8010, Hitachi High-Technologies, Tokyo, Japan) equipped with a Bruker EDS XFlash5060FQ detector. The Archimedes method was performed to measure the relative density with a gravity measurement kit (SMK-401, SHIMADZU Co., Kyoto, Japan). ResiTest8300 (TOYO Co., Aichi-ken, Japan) apparatus was used to measure mobility (μ_H) and carrier density (n_H) at room temperature. In addition, the electrical resistivity (ρ) and Seebeck coefficient (*S*) were also measured by using the ResiTest8300 at temperatures of 80–395 K and by homemade apparatus under an Ar atmosphere at temperatures of 400–800 K. The thermal conductivity (κ_{total}) was measured by using a power efficiency measurement (PEM-2, ULVAC, Inc., Kanagawa, Japan) system and the *ZT* can be calculated by $ZT = S^2 T / (\rho \kappa_{total})$.

3. Results and Discussions

Figure 1 shows the X-ray diffraction (XRD) peaks of $Fe_xNi_{1-x}Si_2$ ($0 \leq x \leq 0.03$) at 300 K within the angles of $20° \leq 2\theta \leq 90°$. Mainly, the β-phase was achieved for $0 \leq x \leq 0.03$; however, a trace of the ε-phase still remained at $2\theta \approx 45.2°$ on the right of the indexed peak (421), as zoomed in on in the inset of Figure 1. The intensity of this ε-phase peak increases with increasing Ni concentration from 0 to 0.03; the low intensity occurred at $x \leq 0.005$. The XRD peaks of our $0 \leq x \leq 0.005$ samples are similar to those of the study of Dąbrowski et al., who reported that a single β-phase was obtained by doping with other impurities, such as aluminum (Al) and phosphorus (P) [26]. Therefore, it is considered that the $0 \leq x \leq 0.005$ samples had very small amounts of the ε-phase.
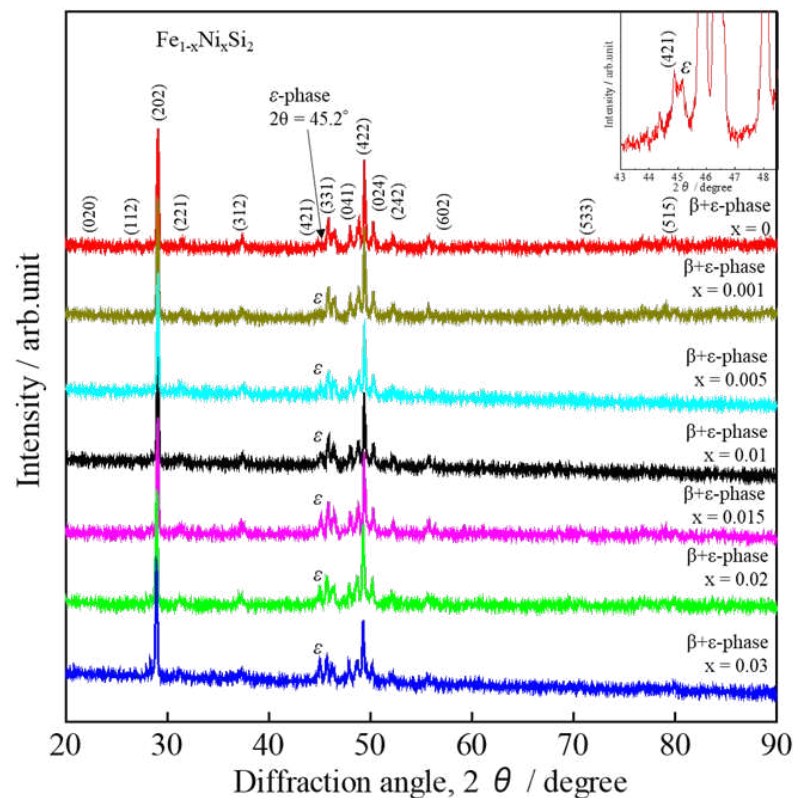

Figure 1. X-ray diffraction patterns of β-$Fe_{1-x}Ni_xSi_2$ ($0 \leq x \leq 0.03$) at room temperature.

Figure 2 shows the SEM images of $Fe_{1-x}Ni_xSi_2$ ($0 \leq x \leq 0.03$) captured at room temperature. The identification of phase transition by using the SEM micrograph can also be found in the previous reports of Dąbrowski et al. [26,31]. Figure 2a shows that before heat treatment, the ε and α-phases were formed at $x = 0$ (the bright grain represents the ε-phase and the dark grain represents α-phase). The white dots are not the microstructures but merely dust contaminated by the polished substrate. After heat treatment, for $0 \leq x \leq 0.005$, the samples were grown in a single β-phase, as shown in Figure 2b–d, and for $0.01 \leq x \leq 0.03$, the samples were grown with the majority of the β-phase and the minority of the ε-phase, as shown in Figure 2e–g. It is observed that the area or amount of the ε-phase increases with increasing Ni addition (x).

To observe the Ni distribution in each phase, the SEM-EDS measurement for elemental analysis was performed for the $0.005 \leq x \leq 0.03$ sample after the heat treatment. As shown in the color mapping of Figure 3, Ni was homogenously distributed for $x = 0.005$ due to the formation of a single β-phase, whereas the Ni-richness was distributed in the area of the ε-phase for $0.01 \leq x \leq 0.03$, as can be seen in the green. This tendency indicates that the semiconducting phase is moderately transformed into the metallic ε-phase by increasing Ni substitution. Furthermore, a portion of the Ni concentration is accumulated

in the grain boundaries between ε-phase and β-phase, probably due to the large particle size of raw material. This issue can probably be solved by ball milling, followed by fast-sintering techniques. By utilizing the ball-milling method, the particle size of Ni can be significantly reduced, and the fast-sintering techniques could help to reduce grain growth. As the particle size reduces, the Ni might more homogenously distribute, leading to simultaneously eliminating the accumulation of Ni and grain growth. In addition, Table 1 also shows the quantitative analysis of the $0.005 \leq x \leq 0.03$ sample. In the area of the β-phase for all samples, the atomic concentration of Fe was approximately 1/3, and that of Si was approximately 2/3. This indicates that Fe:Si ratio is 1:2, corresponding to β-FeSi$_2$. On the other hand, in the area of the ε-phase, the atomic concentration of Fe was approximately $\frac{1}{2}$, and that of Si was also 1/2. This indicates that the Fe:Si ratio is about 1:1, corresponding to ε-FeSi. In the β-phase area of the $0.005 \leq x \leq 0.03$ sample, the actual Ni composition ranged from 0.003(1) to 0.010(4), indicating that the solid solution limit of Ni for β-FeSi$_2$ is lower than $x = 0.01$. When the value is higher than 0.01, it facilitates the formation of the ε-phase. As a result, a single β-phase could be obtained in the $0 \leq x \leq 0.005$ samples, as verified with the SEM image in Figure 2b–d. Moreover, as shown in Table 1, Ni in both β and ε-phases linearly increases with x, but the slope of the ε-phase is around six times that of the β-phase.
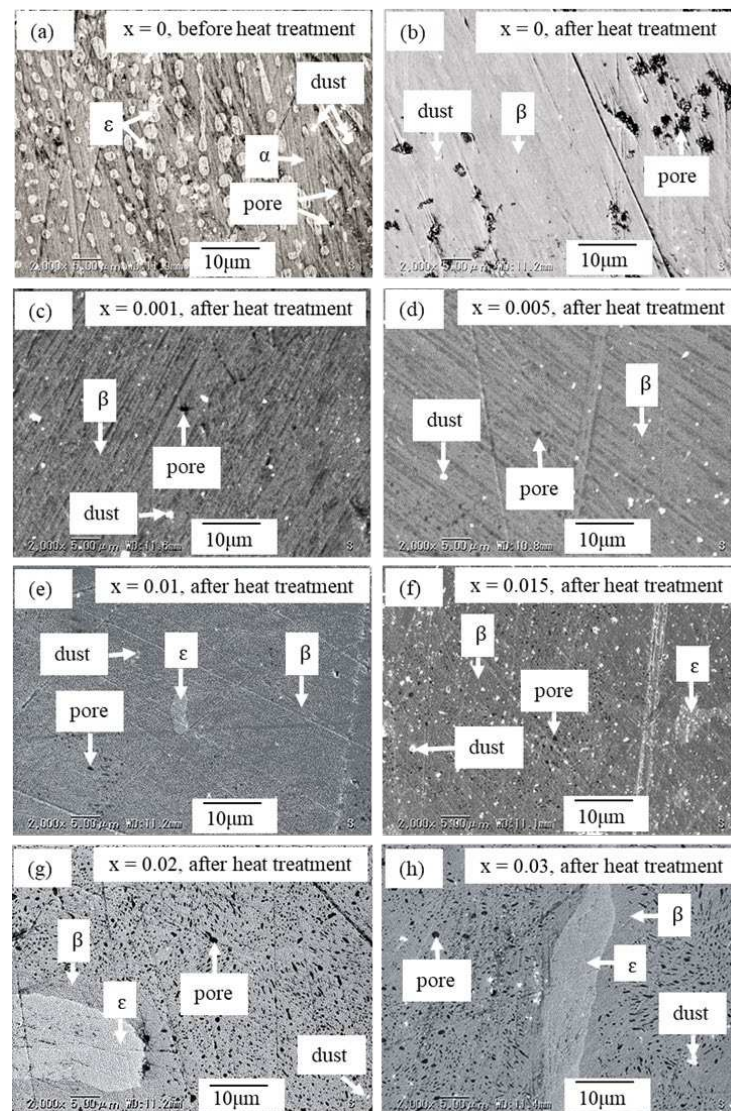
Figure 2. SEM image of β-Fe$_{1-x}$Ni$_x$Si$_2$: (**a**) before heat treatment for $x = 0$, (**b**–**h**) after heat treatment for $0 \leq x \leq 0.03$.

Moreover, Figure 2 shows that pore size after heat treatment is larger than that before heat treatment. This enlargement of pore size happens when the volume β-FeSi$_2$ occupies varies with the volumes of metallic ε and α-phases during the heat-treatment process (ε-FeSi + α-Fe$_2$Si$_5$ → β-FeSi$_2$). However, the relative densities range from 95.6(1)–98.7(1)%, as shown in Table 2. These values are as high as for a sample prepared by hot-pressing (HP) techniques [32], but are relatively higher than those for samples prepared by pulse plasma sintering (PPS) [28] or spark plasma sintering (SPS) [33]. This result suggests that the proposed arc-melting and direct-heat-treatment method is efficient at fabricating a high-relative-density sample that contributes positively to the decrease in electrical resistivity, which is good for TE application. The three dimensions of the orthorhombic crystal structure of β-FeSi$_2$ were provided by our previous report [20].
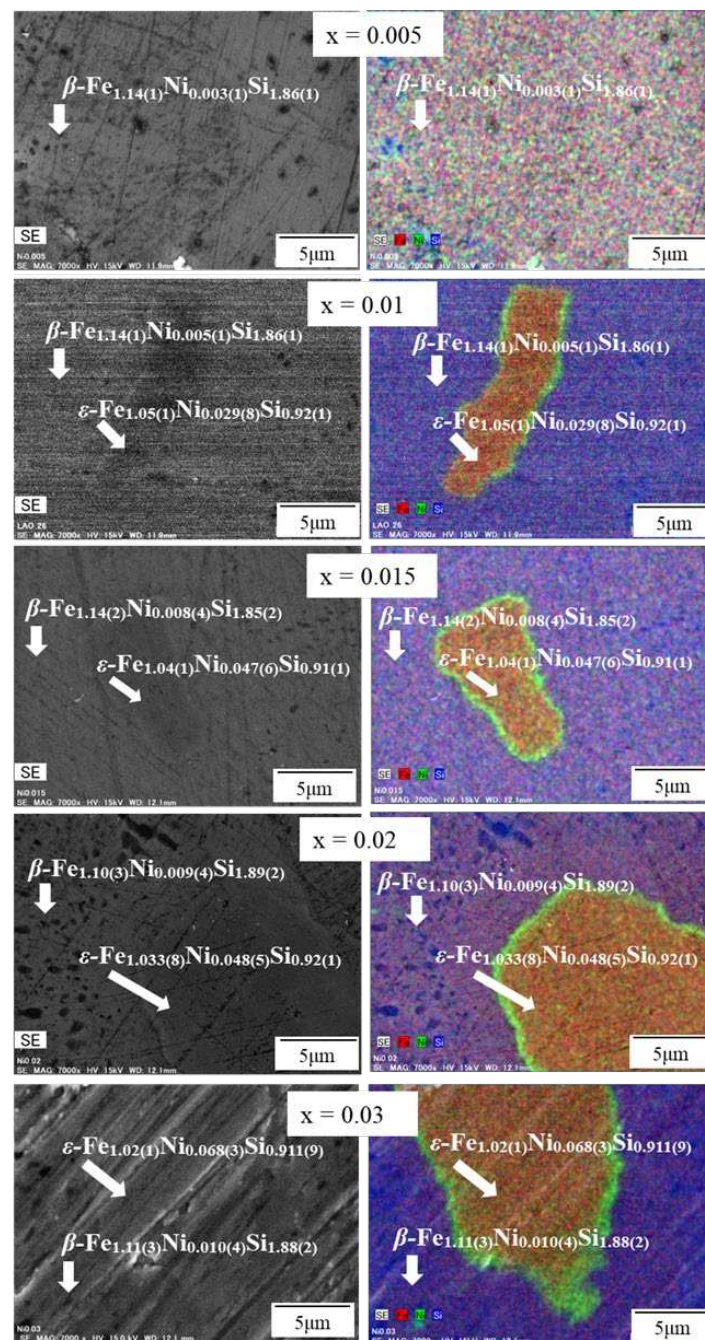

Figure 3. SEM-EDS mapping of β-Fe$_{1-x}$Ni$_x$Si$_2$ ($0.005 \leq x \leq 0.03$). Fe, Ni, and Si are mapped with red, green, and blue, respectively.

Table 1. Elemental composition of β-Fe$_{1-x}$Ni$_x$Si$_2$ ($0.005 \leq x \leq 0.03$) quantified by SEM-EDS analysis.

x	Area	Element	Atomic %	Composition Ratio	Symbol
0.005	β	Fe	38.1(4)	1.14(1)	β-Fe$_{1.14(1)}$Ni$_{0.003(1)}$Si$_{1.86(1)}$
		Ni	0.10(5)	0.003(1)	
		Si	61.8(4)	1.86(1)	
0.01	β	Fe	37.9(5)	1.14(1)	β-Fe$_{1.14(1)}$Ni$_{0.005(1)}$Si$_{1.86(1)}$
		Ni	0.17(4)	0.005(1)	
		Si	62.9(5)	1.86(1)	
	ε	Fe	52.7(4)	1.05(1)	ε-Fe$_{1.05(1)}$Ni$_{0.029(8)}$Si$_{0.92(1)}$
		Ni	1.5(4)	0.029(8)	
		Si	45.8(6)	0.92(1)	
0.015	β	Fe	38.2(6)	1.14(2)	β-Fe$_{1.14(2)}$Ni$_{0.008(4)}$Si$_{1.85(2)}$
		Ni	0.3(1)	0.008(4)	
		Si	61.5(6)	1.85(2)	
	ε	Fe	52.0(6)	1.04(1)	ε-Fe$_{1.04(1)}$Ni$_{0.047(6)}$Si$_{0.91(1)}$
		Ni	2.3(3)	0.047(6)	
		Si	45.7(7)	0.91(1)	
0.02	β	Fe	36.8(9)	1.10(3)	β-Fe$_{1.10(3)}$Ni$_{0.009(4)}$Si$_{1.89(2)}$
		Ni	0.3(1)	0.009(4)	
		Si	62.9(8)	1.89(2)	
	ε	Fe	51.7(7)	1.033(8)	ε-Fe$_{1.033(8)}$Ni$_{0.048(5)}$Si$_{0.92(1)}$
		Ni	2.4(2)	0.048(5)	
		Si	45.9(6)	0.92(1)	
0.03	β	Fe	37.1(9)	1.11(3)	β-Fe$_{1.11(3)}$Ni$_{0.010(4)}$Si$_{1.88(2)}$
		Ni	0.3(1)	0.010(4)	
		Si	62.5(8)	1.88(2)	
	ε	Fe	51.1(5)	1.02(1)	ε-Fe$_{1.02(1)}$Ni$_{0.068(3)}$Si$_{0.911(9)}$
		Ni	3.4(2)	0.068(3)	
		Si	45.5(4)	0.911(9)	

Table 2. Summary of thermoelectric properties of β-Fe$_{1-x}$Ni$_x$Si$_2$ ($0 \leq x \leq 0.03$) at 300 K, where L_O, r = $-1/2$, n_H, μ_H, S, ρ, and κ are Lorenz number, scattering factor (for acoustic phonon scattering), carrier density, mobility, Seebeck coefficient, electrical resistivity, and thermal conductivity, respectively.

x	L_O [V^{2}K^{-2}]	r	n_H [cm^{-3}]	μ_H [cm^{2}V^{-1}s^{-1}]	$\|S\|$ [μVK^{-1}]	ρ [Ωcm]	κ [Wm^{-1}K^{-1}]	Relative Density [%]
0	1.792×10^{-8}	$-1/2$	$2.3(2) \times 10^{16}$	37(4)	127	7.10	7.16	98.0(1)
0.001	1.624×10^{-8}	$-1/2$	$1.2(4) \times 10^{17}$	35(7)	393	1.39	8.25	98.3(1)
0.005	1.656×10^{-8}	$-1/2$	$2.6(2) \times 10^{17}$	34(3)	194	0.69	8.57	96.24(8)
0.01	1.648×10^{-8}	$-1/2$	$3.2(7) \times 10^{17}$	27(5)	205	0.69	8.44	97.5(3)
0.015	1.674×10^{-8}	$-1/2$	$4.8(4) \times 10^{17}$	20(1)	176	0.63	7.27	98.7(1)
0.02	1.766×10^{-8}	$-1/2$	$1.2(4) \times 10^{18}$	11(3)	135	0.45	7.12	95.6(2)
0.03	2.139×10^{-8}	$-1/2$	$2.3(2) \times 10^{18}$	10(1)	62	0.26	6.18	95.6(1)

The bonds of the Fe1 and sites are formed geometrically in eight coordinates, four each to Si1 and Si2, and the bonds of Fe–Si vary in length from 2.361(5) to 2.402(6) Å and from 2.282(5) to 2.415(4) Å, respectively.

The Rietveld analysis of β-Fe$_{0.995}$Ni$_{0.005}$Si$_2$ after heat treatment is shown in Figure A1 (Appendix A). The calculated data, experimental data, and difference between the data, are represented by green, red, and blue lines, respectively. According to the analysis, it is considered that after the process of heat treatment, the sample is successfully grown in the β-phase with a trace of the metallic ε-phase.

Therefore, the result of the Rietveld analysis agrees with that of the SEM image. The orthorhombic structure (*Cmce* space group) was chosen for Rietveld analysis. As Ni was

partially substituted into the Fe sites, 1−x was assigned as the occupied rate of Fe1 and Fe2, and x was assigned as the occupied rate of Ni1 and Ni2. In addition, both the Fe site and Si site were assigned with the isotropic atomic displacement *B* with the value of 1.0 Å². A split pseudo-Voigt function was used to fit the Bragg peak profiles. A summary of the structural parameters, which were calculated by the Rietveld analysis, is reported in Table A1 (Appendix B). The lattice constants (*a*, *b*, *c*), interact atomic distances (Si-Fe), interacting atomic angles (Fe-Si-Fe), and reliability factor for weight diffraction patterns (R_{wp}) with x dependences are plotted in Figure 4. In Figure 4a, the variations in lattice constants *a*, *b*, and *c* with x are negligible. In addition, as shown in Table A1, the change in unit-cell volume (*V*) is almost within the error range. The effect of Ni substitutions is probably not significant for the lattice constants due to the low solubility limit of Ni. Figure 4b shows that the atomic distances of Si1-Fe1 and Si1-Fe2 tend to slightly rise with increasing x, though there is no significant change in Si2-Fe1 or Si2-Fe2 with x. In addition, the interactive atomic angles of both Fe1-Si1-Fe1 and Fe2-Si2-Fe2 slightly rise with x, but those of both Fe1-Si2-Fe1 and Fe1-Si2-Fe1 slightly decline as x increases, as shown in Figure 4c. It is considered that both Fe1 and Fe2 are slightly changed with Ni addition. Therefore, the Ni population should equally occupy both Fe1 and Fe2 sites, which is similar to a previous study wherein Co was doped into the *β*-FeSi₂ system [20,34]. Figure 4d shows the reliability factor R_{wp} with x dependences. The R_{wp} value for x = 0 is about 3.316%, indicating a good fit between the observed and computed intensities. However, as x increases, the R_{wp} moderately increases, probably due to the increasing amount of the *ε*-phase, which is verified with XRD patterns in Figure 1 and the SEM image in Figure 2.
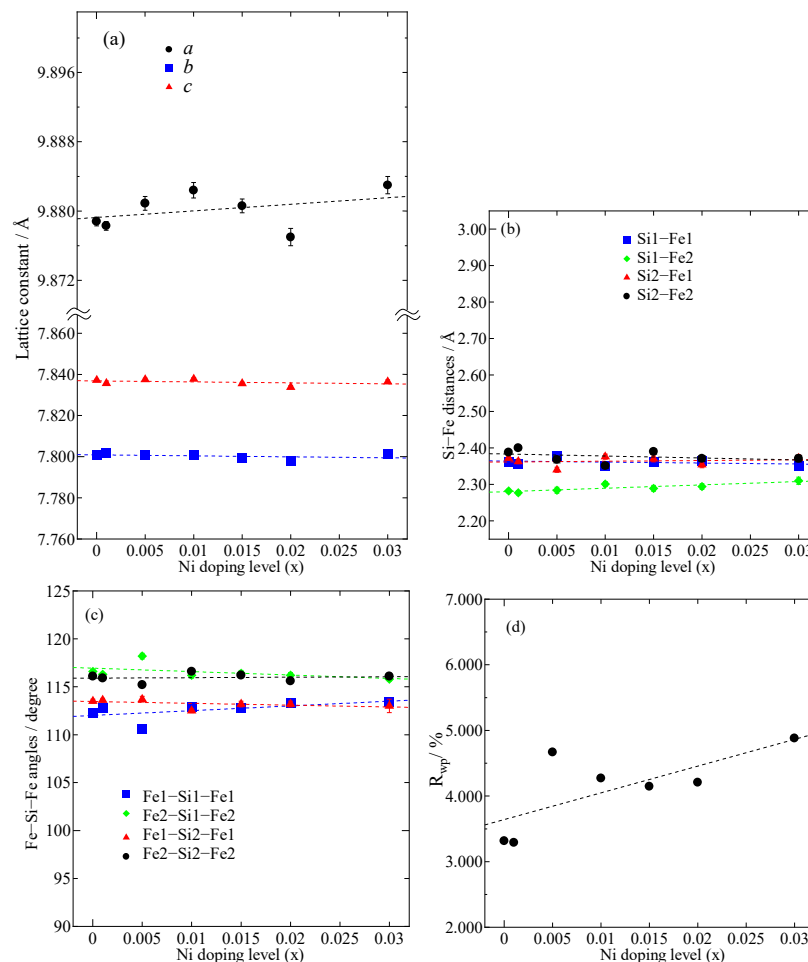

Figure 4. (**a**) Lattice constants *a*, *b*, *c*; (**b**) interactive atomic distances of Fe-Si, (**c**) interactive atomic angles of Fe-Si-Fe, and (**d**) reliability factor R_{wp} for β-Fe$_{1−x}$Ni$_x$Si$_2$ (0 ≤ x ≤ 0.03) at room temperature.

The electrical resistivity (ρ) with respect to the temperature dependence of $Fe_{1-x}Ni_xSi_2$ is shown in Figure 5. The ρ significantly decreases as Ni content increases from x = 0 to x = 0.03. The decrease in ρ is mainly caused by the increases in ε-phase and carrier concentration (n_H), as shown in the inset of Figure 5. This tendency can be explained by Drude's theory in Equation (1):

$$\rho = n_H^{-1}|e|^{-1}\mu_H^{-1} \tag{1}$$

where e and μ_H are elementary charge and carrier mobility, respectively [35]. Equation (1) expresses that ρ is inversely proportional to n_H. Therefore, as n_H increases, ρ can be effectively obtained. In Table 2, the ρ of the non-doped sample is 7.10 Ωcm with the n_H of only around $1.3(2) \times 10^{16} cm^{-3}$. As x increases from 0.001 to 0.03, the ρ remarkably decreases from 1.39 to 0.26 Ωcm due to the increase in n_H from $1.2(4) \times 10^{17}$ to $2.3(2) \times 10^{18}$ cm^{-3}. Furthermore, the increase in the ε-phase with Ni substitution, as discussed for the microstructures above, should also contribute to the reduction in ρ. For x = 0.01, the ρ value of our sample was almost similar to that of the one Tani and Kido prepared by pressure-sintering techniques [30]. However, for x = 0.03, the ρ of our sample was about two times lower due to the higher μ_H. The μ_H of our sample was 10(1) $cm^2V^{-1}s^{-1}$, and that of their sample was only around 0.27 $cm^2V^{-1}s^{-1}$. If we compare another dopant, cobalt (Co), at the same doping level, the Ni-substituted material has a much higher value of ρ than the Co-substituted materials. This is because Co has a higher solid solution limit in β-FeSi$_2$; its value is up to 0.116, as reported by Kojima et al. [36]. In addition, Nagai et al. reported that the ρ of the x = 0.06 thin film was 0.076 Ωcm. Such a low value of ρ in a thin-film sample should be mainly affected by the large μ_H. It is considered that the ρ of the bulk sample prepared by the arc-melting method should drastically decrease if the doping amount is up to x = 0.06 due to the increase in n_H; however, the thermoelectric power will be deteriorated due to the effect of the metallic ε-phase.
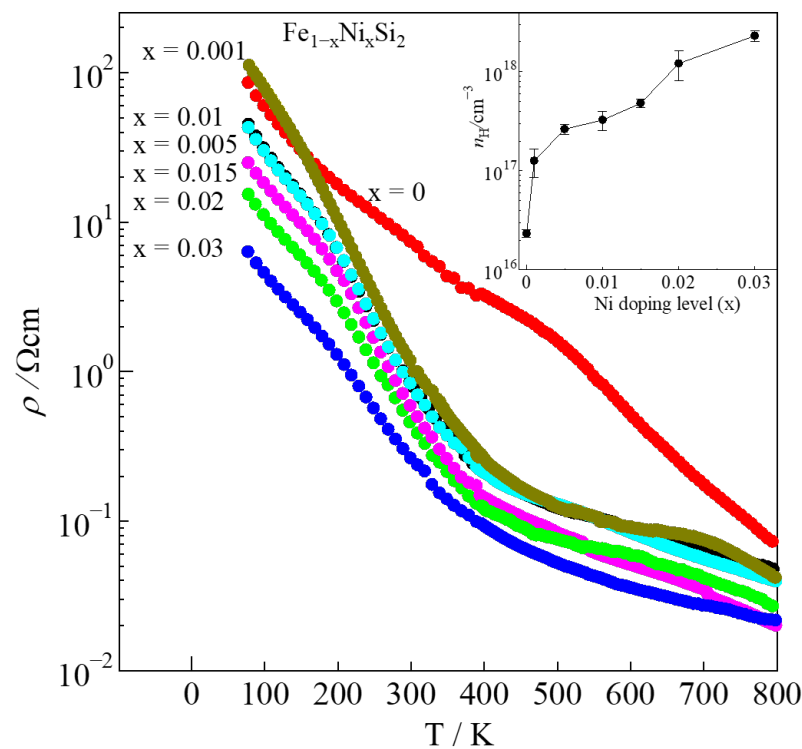

Figure 5. Electrical resistivity of β-$Fe_{1-x}Ni_xSi_2$ ($0 \le x \le 0.03$) with respect to temperature, where the carrier concentration, n_H, at 300 K is plotted in the inset.

The Seebeck coefficient (S) with temperature dependence is shown in Figure 6. The $|S|$ of the non-doped sample (x = 0) remarkably decreases from about 290 μVK^{-1} to

approximately 0 μVK^{-1} as the temperature increases from 420 to 800 K. It is considered that the bipolar effect dominates at high-temperature regions in pristine β-FeSi$_2$ due to low carrier density. For the Ni-doped β-FeSi$_2$ system, the *S* is positive at temperatures 80–115 K and 80–195 K for x = 0.001 and 0.03, respectively, indicating the p-type materials. At higher temperatures, the *S* becomes negative, indicating an n-type conduction material. This result is consistent with that of Tani and Kido [30], who also reported that the sign of the Hall coefficient (R_H) changes from positive to negative at 160 K. It is considered that conduction is dominated by both holes and electrons, and its ratio varies depending on temperature. In addition, as x increases, the |S| becomes more stable from room temperature to 800 K. This tendency suggests that the bipolar effect is remarkably reduced with Ni substitution due to the increase in n_H. The bipolar effect was reduced by Ni doping; however, at high temperatures, it was not completely eliminated. This is probably due to the much lower actual Ni doping concentration in the β-phase. The increase in n_H contributes to the reduction in |S|. The relationship between |S| and n_H can be expressed by Mott's formula:

$$S = \frac{k_B^2 T}{3|e|\hbar^2} m^* \left(\frac{\pi}{3n_H} \right)^{2/3} \qquad (2)$$

where k_B, *T*, *e*, $\hbar$, m^*, and n_H are Boltzmann constant, temperature, elementary charge, Planck constant, effective mass, and carrier concentration, respectively [37]. Equation (2) indicates that the |S| is inversely proportional to n_H; therefore, as can be seen in Figure 6, for $0.001 \leq x \leq 0.03$, the |S| of the Ni-doped samples decreases with x. Furthermore, the inset of Figure 6 shows that μ_H decreases with x, probably owing to the difference in the effective mass between the electron and the hole. This tendency can be expressed by Equation (3):

$$m^* = \frac{e\tau}{\mu_H} \qquad (3)$$

where *e*, τ, and μ_H are elementary charge, scattering time, and mobility, respectively [35]. When the effective mass of the electron is larger than that of the hole, the mobility of the electron is lower. As shown in Figure A2 (Appendix A), for $0.001 \leq x \leq 0.03$, the |S| decreases with n_H, and the tendency of the experimental values of |S| fits with that of the calculated values (solid black curve, in the case of $m^* = 0.1\ m_e$) using the Mott's formula in Equation (2). It is confirmed that Mott's theory implies for $0.001 \leq x \leq 0.03$. For $0 \leq x < 0.001$, the experimental value of |S| is out of the fitting curve; therefore, this might be possibly described by a two-carrier model [38]. The highest value of |S| was obtained for the x = 0.001 sample with the value of 450 μVK^{-1} at 450 K.

Figure 7 shows the power factor (*PF*) with temperature dependence. The *PF* is calculated by $PF = S^2\rho^{-1}$. The improvement in *PF* contributes positively to enhancing TE performance (*ZT*). The *PF* of the non-doped sample exhibited the highest value of around 3.5 $\mu Wm^{-1}K^{-2}$ at around 450 K, as shown in the inset of Figure 7. By doping with Ni, the *PF* can be significantly improved; the maximum value was around 200 $\mu Wm^{-1}K^{-2}$ at 600 K, achieved by the x = 0.001 sample. The enhancement in *PF* is caused not only by the remarkable increase in, *S* but also by the reduction in ρ. Compared to previous work reported by Komabayashi et al., the *PF* of thin-film x = 0.06 was 17 $\mu Wm^{-1}K^{-2}$ at 300 K [28]. This value is similar to that of our bulk x = 0.001 sample with the *PF* of about 13 $\mu Wm^{-1}K^{-2}$ at 300 K. The thin-film sample usually had a much lower ρ than that of the bulk sample, which provided a better *PF*. However, the high value of |S| for our bulk sample also increased the *PF*, which is comparable to that of the thin-film sample. In addition, Nagai et al. reported that the highest *PF* of the bulk x = 0.01 samples prepared by mechanical milling and hot pressing was about 50 $\mu Wm^{-1}K^{-2}$ at 650 K [29], whereas that of our x = 0.01 sample prepared by arc-melting was about 130 $\mu Wm^{-1}K^{-2}$ at 750 K. The higher *PF* in our sample is owed to the larger |S|. It is considered that our sample had a lower ε-phase amount as a result of the heat-treatment process, as that was not applied to

their sample. This might be a reason why the $|S|$ of their sample was lower. Therefore, heat treatment is necessary for the fabrication of β-FeSi$_2$ for TE applications.
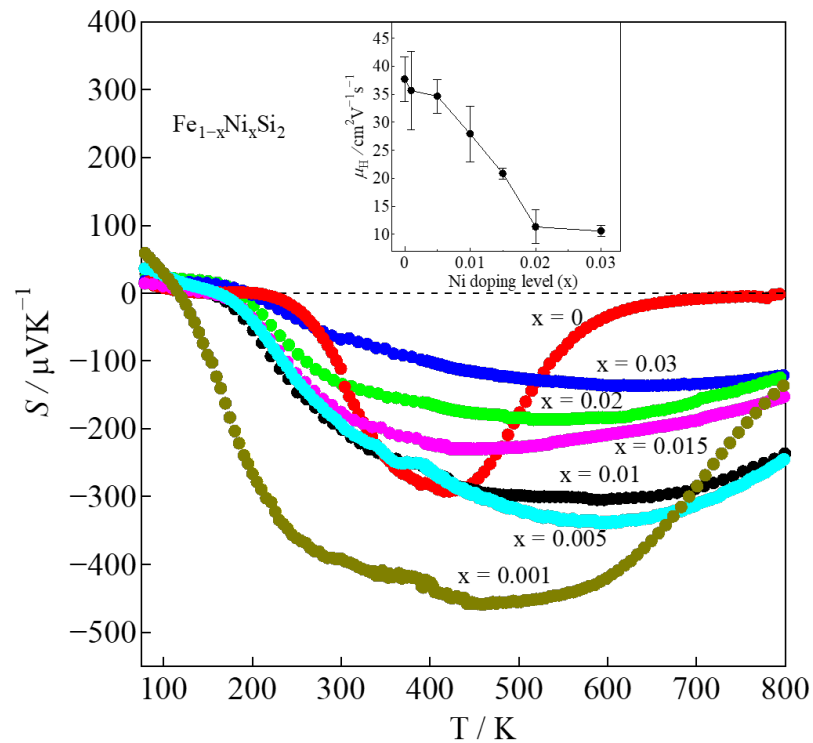

Figure 6. Seebeck coefficient of β-Fe$_{1-x}$Ni$_x$Si$_2$ ($0 \leq x \leq 0.03$) with respect to temperature, where the carrier mobility, μ_{H}, at 300 K is plotted in the inset.
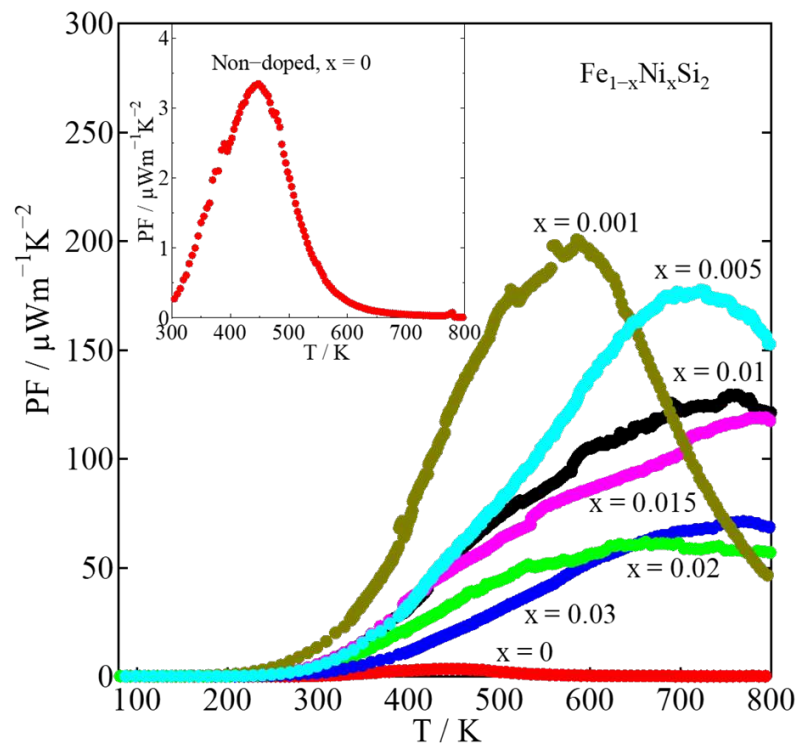
Figure 7. Power factor (*PF*) of β-Fe$_{1-x}$Ni$_x$Si$_2$ ($0 \leq x \leq 0.03$) with respect to temperature, where the inset plots the data of x = 0.

The total thermal conductivity ($\kappa_{\text{total}} = \kappa_1 + \kappa_e$, where κ_1 and κ_e are the lattice and electronic thermal conductivity, respectively) of all samples is plotted in Figure 8. It is shown that the κ_{total} of Ni-doped samples is slightly higher than that of the on-doped one. This is probably because of the increase in the metallic ε-phase with increasing Ni content, as can be proved by XRD patterns and SEM-EDS analysis. As shown in the inset of Figure 8, the electronic thermal conductivity (κ_e) increased with x due to the decrease in ρ. The κ_e was calculated by the Wiedemann–Franz law ($\kappa_e = L_O T / \rho$, where L_O is the Lorenz number). The L_O was calculated by the measured Seebeck coefficient $|S|$ in the case of acoustic phonon scattering (r = $-1/2$). Equation (4) explains the relationship between L_O and *r*:

$$L_O = \left(\frac{k_B}{e}\right)^2 \left[\frac{\left(r+\frac{7}{2}\right)F_{r+\frac{5}{2}}(\eta)}{\left(r+\frac{3}{2}\right)F_{r+\frac{1}{2}}(\eta)} - \left\{ \frac{\left(r+\frac{5}{2}\right)F_{r+\frac{3}{2}}(\eta)}{\left(r+\frac{3}{2}\right)F_{r+\frac{1}{2}}(\eta)} \right\}^2 \right] \tag{4}$$

where the function is given as: $F_n(\eta) = \int_0^\infty \frac{\chi^n}{1+e^{\chi-\eta}} d\chi$, $\chi = \frac{E}{k_B T}$, $\eta = \frac{E_F}{k_B T}$ and E_F is Fermi energy [39]. Table 2 shows that the values of L_O increase with x for $0.001 \leq x \leq 0.03$. This tendency shows that the β-phase moderately transforms into the ε-phase as the level of Ni doping increases. The increase in L_O also contributes to the high κ_e because of its proportionality.

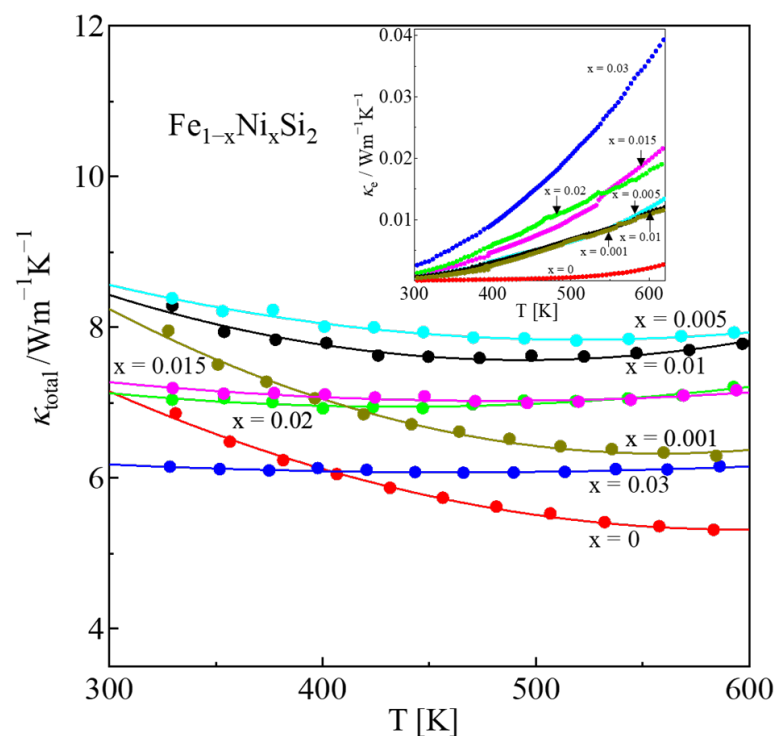**Figure 8.** Thermal conductivity ($\kappa_{\text{total}} = \kappa_L + \kappa_e$) of β-Fe$_{1-x}Ni_xSi_2$ ($0 \leq x \leq 0.03$) with respect to temperature, where the inset plots the electronic thermal conductivity ($\kappa_e = L_o T / \rho$).

The *ZT* value with temperature dependences is plotted in Figure 9. In addition, the inset of Figure 9 shows that the x = 0 sample had the highest *ZT* value of 2.6×10^{-4} at the temperature of 450 K. If we compare the *ZT* value of pristine material to Ni-doped materials, its value is very low. In the Ni-doped system, the maximum *ZT* of around 0.019 at 600 K was obtained in x = 0.001 owing to the enhancement of the power factor. When x is higher than 0.001, the *ZT* is decreased due to the reduction in $|S|$ caused by the increased amount of metallic ε-phase. Therefore, it is considered that for Ni-doped β-FeSi$_2$, the low doping amount, below 1%, is more effective at improving the TE properties.
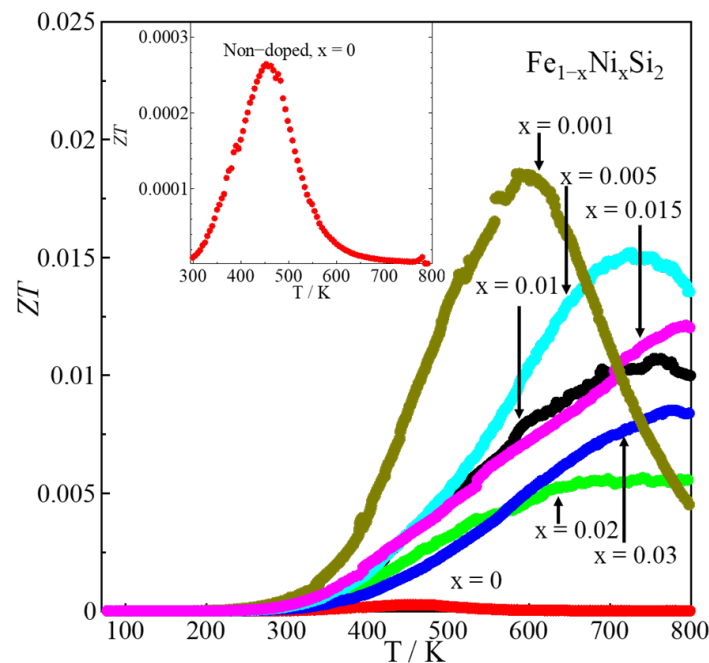
Figure 9. *ZT* of β-Fe$_{1-x}$Ni$_x$Si$_2$ ($0 \leq x \leq 0.03$) with respect to temperature, where the inset plots the data for x = 0.

4. Conclusions

Thermoelectric (TE) materials β-Fe$_{1-x}$Ni$_x$Si$_2$ were fabricated for $0 \leq x \leq 0.03$ by the conventional arc-melting method, followed by a heat treatment and annealing process. Traces of the ε-phase were formed for all samples; the lowest amount of it was obtained at $x \leq 0.005$. The solid solution limit of Ni in the β-phase is below x = 0.01, and the ε-phase increases with increasing Ni concentration. As x increases, the electrical resistivity (ρ) and Seebeck coefficient $|S|$ decrease, owing to the increases in ε-phase and carrier density. As a result, the optimum doping amount to achieve a maximum power factor (*PF*) of around 200 μWm^{-1}K^{-2} was obtained in the x = 0.001 sample due to significant enhancement in $|S|$. The *PF* value of this sample was comparable to that of the thin-film sample reported by Komabayashi et al. [28]. However, this value is higher than that of the hot-pressed sample reported by Nagai et al. [29], resulting from the improvement in $|S|$. The improvement in *PF* led to obtaining the *ZT* of 0.019 at 600 K in the same x = 0.001 sample. It would be worth investigating a method to increase Ni's solubility in β-FeSi$_2$. As Ni solubility increases, the ε-phase can be reduced, resulting in an improvement in *S* and a decrease in thermal conductivity (κ). Therefore, *ZT* can be more significantly enhanced, making the material suitable for industrial waste heat recovery in mid–high temperature applications.

Author Contributions: Conceptualization, S.S., H.N. and Y.O.; methodology, S.S. and S.O.; formal analysis, S.S., S.O., H.N. and Y.O.; investigation, S.S. and S.O.; resources, H.N., and Y.O.; data curation, S.S. and S.O., writing—original draft preparation, S.S.; writing—review and editing, S.S. and H.N. All authors have read and agreed to the published version of the manuscript.

Institutional Review Board Statement: Not applicable.

Informed Consent Statement: Not applicable.

Data Availability Statement: Not applicable.

Conflicts of Interest: The authors declare no conflict of interest.

Appendix A

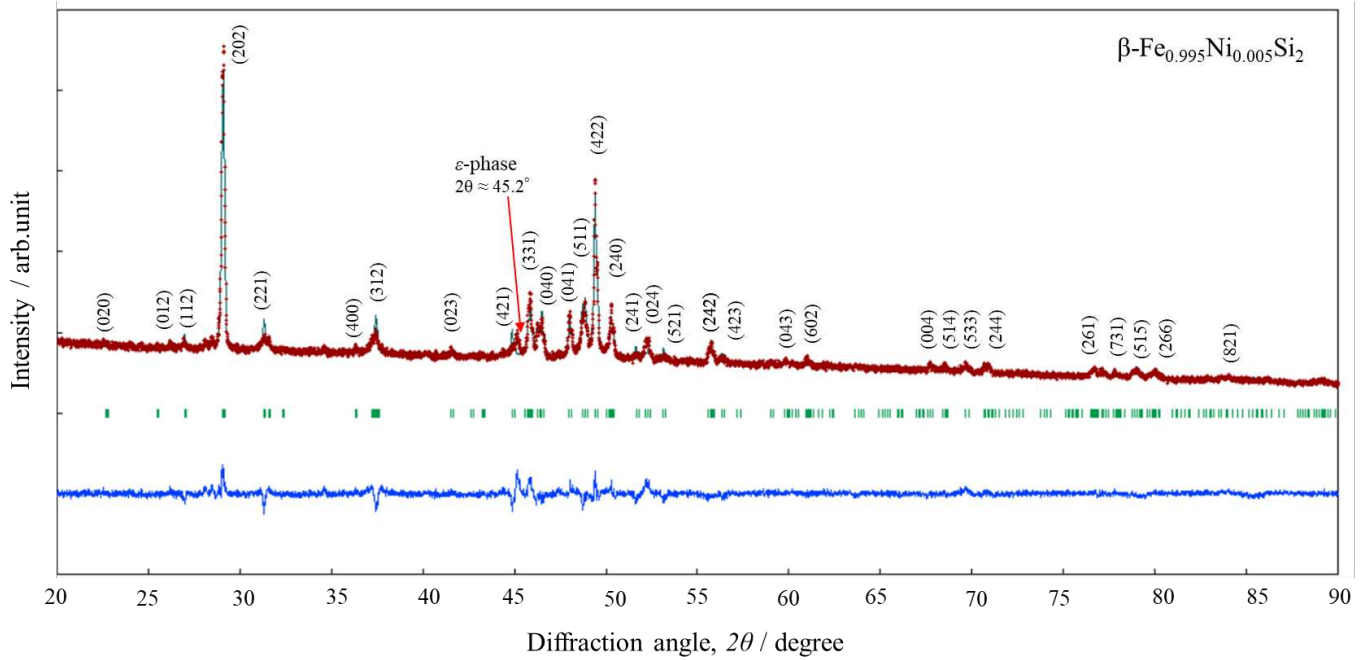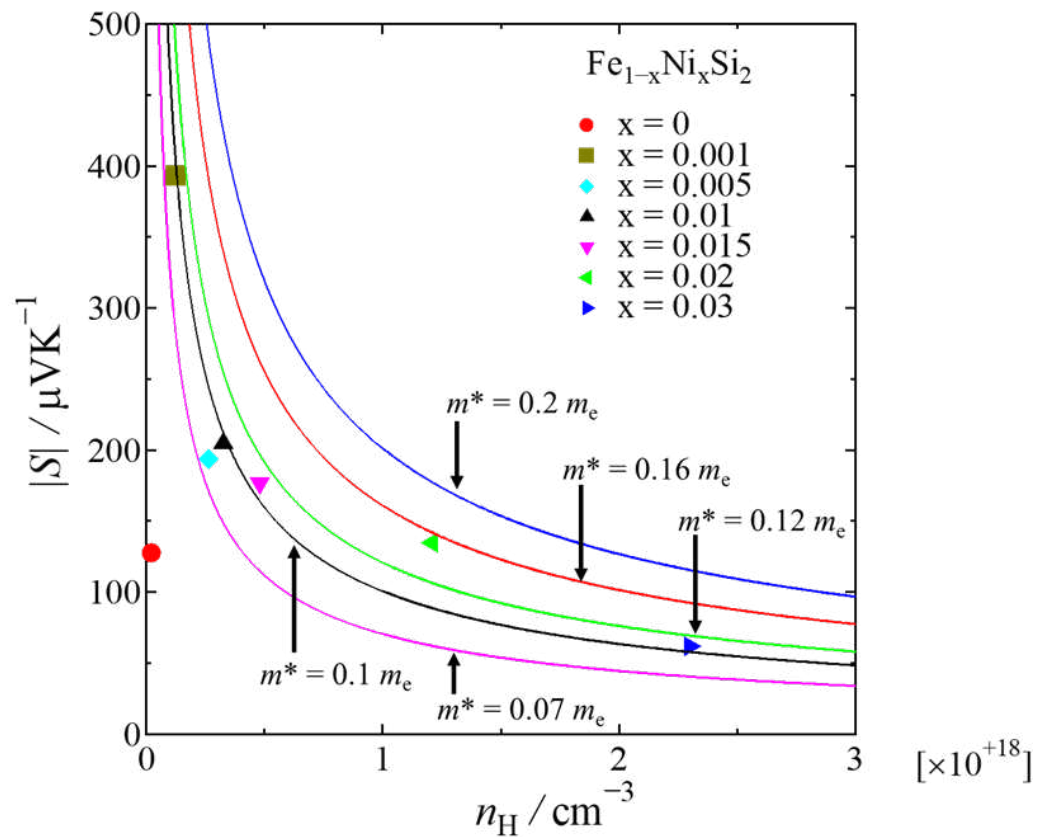**Figure A1.** Rietveld analysis of β-Fe$_{0.995}$Ni$_{0.005}$Si$_2$.

Figure A2. Absolute Seebeck coefficient with respect to carrier concentration at room temperature, where the solid curves represent the calculated data estimated by using Mott's formula at various effective masses ($m^* = x\, m_e$, where x is variable and m_e is the static mass of electron, i.e., 9.10938×10^{-31} kg).

Appendix B

Table A1. Crystal-structure parameters of β-Fe$_{1-x}$Ni$_x$Si$_2$ ($0 \leq x \leq 0.03$) at room temperature.

Samples		Fe$_{1-x}$Ni$_x$Si$_2$						
Composition, x		0	0.001	0.005	0.01	0.015	0.02	0.03
Space Group		*Cmce*	*Cmce*	*Cmce*	*Cmce*	*Cmce*	*Cmce*	*Cmce*
a (Å)		9.8788(5)	9.8783(5)	9.8809(8)	9.8824(9)	9.8806(8)	9.877(1)	9.883(1)
b (Å)		7.8008(4)	7.8016(4)	7.8009(7)	7.8008(7)	7.7993(6)	7.7978(8)	7.8011(9)
c (Å)		7.8372(4)	7.8357(4)	7.8375(7)	7.8378(7)	7.8356(6)	7.8338(8)	7.8365(9)
V (Å^3)		603.96(5)	603.88(5)	604.12(9)	604.23(9)	603.83(8)	603.4(1)	604.1(1)
Fe1	*x*	0.2160(2)	0.2163(3)	0.2178(4)	0.2173(3)	0.2170(4)	0.2170(4)	0.2179(5)
	y	0	0	0	0	0	0	0
	z	0	0	0	0	0	0	0
	B (Å^2)	0.1	0.1	0.1	0.1	0.1	0.1	0.1
	g	1.000	0.999	0.995	0.990	0.985	0.980	0.970
Ni1	*x*	N/A	0.2163(3)	0.2178(4)	0.2173(3)	0.2170(4)	0.2170(4)	0.2179(5)
	y	N/A	0	0	0	0	0	0
	z	N/A	0	0	0	0	0	0
	B (Å^2)	N/A	0.1	0.1	0.1	0.1	0.1	0.1
	g	N/A	0.001	0.005	0.010	0.015	0.020	0.030
Fe2	*x*	1/2	1/2	1/2	1/2	1/2	1/2	1/2
	y	0.3014(4)	0.3019(4)	0.2987(6)	0.3015(5)	0.3034(5)	0.3031(6)	0.3036(7)
	z	0.1940(4)	0.1943(4)	0.1967(5)	0.1970(5)	0.1944(5)	0.1962(5)	0.1965(6)
	B (Å^2)	0.1	0.1	0.1	0.1	0.1	0.1	0.1
	g	1.000	0.999	0.995	0.990	0.985	0.980	0.970
Ni2	*x*	N/A	1/2	1/2	1/2	1/2	1/2	1/2
	y	N/A	0.3019(4)	0.2987(6)	0.3015(5)	0.3034(5)	0.3031(6)	0.3036(7)
	z	N/A	0.1943(4)	0.1967(5)	0.1970(5)	0.1944(5)	0.1962(5)	0.1965(6)
	B (Å^2)	N/A	0.1	0.1	0.1	0.1	0.1	0.1
	g	N/A	0.001	0.005	0.010	0.015	0.020	0.030
Si1	*x*	0.1217(5)	0.1227(6)	0.1178(8)	0.1231(8)	0.1228(8)	0.1236(9)	0.124(1)
	y	0.2811(7)	0.2801(7)	0.281(1)	0.2795(9)	0.2784(9)	0.276(1)	0.277(1)
	z	0.0394(4)	0.0377(4)	0.0410(6)	0.0388(6)	0.0394(6)	0.0385(6)	0.0404(8)
	B (Å^2)	0.3	0.3	0.3	0.3	0.3	0.3	0.3
	g	1.0	1.0	1.0	1.0	1.0	1.0	1.0
Si2	*x*	0.3761(5)	0.3758(6)	0.3742(8)	0.3775(7)	0.3764(8)	0.3755(8)	0.3762(9)
	y	0.0399(5)	0.0387(6)	0.0434(8)	0.0442(7)	0.0414(7)	0.0442(8)	0.0445(9)
	z	0.2220(6)	0.2219(7)	0.2200(9)	0.2217(9)	0.2222(9)	0.2200(9)	0.223(1)
	B (Å^2)	0.3	0.3	0.3	0.3	0.3	0.3	0.3
	g	1.0	1.0	1.0	1.0	1.0	1.0	1.0
R_{wp} (%)		3.316	3.292	4.669	4.272	4.148	4.209	4.881
R_P (%)		2.108	2.107	3.397	3.012	2.773	2.786	3.163
R_R (%)		29.041	30.762	38.361	35.726	36.636	36.753	40.663
R_e (%)		0.792	1.429	1.222	1.069	0.922	0.883	1.029
R_B (%)		8.543	9.144	10.839	10.024	10.650	9.684	11.392
R_F (%)		8.603	8.788	8.217	8.323	9.418	7.582	8.542
$S = R_{wp}/R_e$		4.187	2.305	3.821	3.996	4.499	4.767	4.743
Si1—Fe1/Ni1 (Å)		2.361(5)	2.357(6)	2.377(8)	2.352(7)	2.363(7)	2.365(9)	2.351(9)
Si1—Fe1/Ni1 (Å)		2.402(6)	2.391(6)	2.426(9)	2.390(8)	2.382(8)	2.366(8)	2.37(1)
Si1—Fe2/Ni2 (Å)		2.282(5)	2.277(6)	2.284(8)	2.301(7)	2.289(8)	2.294(8)	2.31(1)
Si1—Fe2/Ni2 (Å)		2.415(4)	2.430(5)	2.366(6)	2.407(6)	2.420(6)	2.418(7)	2.410(9)
Fe1/Ni1—Si1—Fe1/Ni1 (deg.)		112.3(2)	112.8(2)	110.6(3)	112.9(3)	112.8(3)	113.3(3)	113.4(4)
Fe2/Ni2—Si1—Fe2/Ni2 (deg.)		116.6(2)	116.3(2)	118.2(3)	116.2(3)	116.4(3)	116.2(3)	115.8(2)
Si2—Fe1/Ni1 (Å)		2.372(5)	2.363(6)	2.340(7)	2.376(7)	2.370(8)	2.354(8)	2.372(9)
Si2—Fe1/Ni1 (Å)		2.381(5)	2.386(6)	2.399(8)	2.399(7)	2.386(7)	2.400(8)	2.385(9)
Si2—Fe2/Ni2 (Å)		2.322(6)	2.314(7)	2.355(8)	2.335(9)	2.315(9)	2.34(1)	2.32(1)
Si2—Fe2/Ni2 (Å)		2.388(5)	2.400(5)	2.368(9)	2.351(7)	2.390(7)	2.371(8)	2.371(9)
Fe1/Ni1—Si2—Fe1/Ni1 (deg.)		113.5(2)	113.6(2)	113.7(3)	112.5(2)	113.2(3)	113.2(3)	113.0(7)
Fe2/Ni2—Si2—Fe2/Ni2 (deg.)		116.1(2)	115.9(2)	115.2(3)	116.6(2)	116.2(3)	115.6(3)	116.1(3)

References

1. Chen, X.Q.; Yang, J.P.; Wu, T.; Li, L.; Luo, W.; Jiang, W.; Wang, L.J. Nanostructured Binary Copper Chalcogenides: Synthesis Strategies and Common Applications. *Nanoscale* **2018**, *10*, 15130–15163. [CrossRef] [PubMed]
2. Chen, X.Q.; Zhang, H.; Zhao, Y.Y.; Liu, W.D.; Dai, W.; Lu, X.F.; Wu, C.; Luo, W.; Fan, Y.C.; Wang, L.J.; et al. Carbon-Encapsulated Copper Sulfide Leading to Enhanced Thermoelectric Properties. *ACS Appl. Mater. Interfaces* **2019**, *11*, 22457–22463. [CrossRef] [PubMed]
3. Chen, X.Q.; Fan, S.J.; Han, C.; Wu, T.; Wang, L.J.; Jian, W.; Dai, W.; Yang, J.P. Multiscale architectures boosting thermoelectric performance of copper sulfide compound. *Rare Met.* **2021**, *40*, 2017–2025. [CrossRef] [PubMed]
4. Wever, F.; Moller, H. The crystal structure of iron silicide, FeSi. *Z. Kristallogr.* **1930**, *75*, 362–365.
5. Pauling, L.; Soldate, A.M. The nature of the bonds in the iron silicide, FeSi, and related crystals. *Acta Cryst.* **1948**, *1*, 212–216. [CrossRef]
6. Sidorenko, F.A.; Gel'd, P.V.; Shumilov, M.A. Investigation of α-leboite transition. *Fiz. Met. Metalloved.* **1960**, *6*, 861.
7. Sakata, T.; Sakai, Y.; Yoshino, H.; Fujii, H.; Nishida, I. Studies on the formation of $FeSi_2$ from the $FeSi$-Fe_2Si_5 eutectic. *J. Less Common Met.* **1978**, *61*, 301–308. [CrossRef]
8. Dusausoy, Y.; Protas, J.; Wandji, R.; Roques, B. Structure cristalline du disiliciure de fer, $FeSi_2$ β. *Acta Cryst.* **1971**, *B27*, 1209–1218. [CrossRef]
9. Piton, J.P.; Fay, M.F. Phase changes in iron–silicon alloys around the composition $FeSi_2$. *C. R. Acad. Sci.* **1968**, *C266*, 514–516.
10. Clark, S.J.; Al-Allak, H.M.; Brand, S.; Abram, R.A. Structure and electronic properties of $FeSi_2$. *Phys. Rev. B* **1998**, *58*, 10389–10393. [CrossRef]
11. Watanabe, T.; Hasaka, M.; Morimura, T.; Nakashima, H. Thermoelectric properties of the Co-doped β-$FeSi_2$ mixed with Ag. *J. Alloys Compd.* **2006**, *417*, 241–244. [CrossRef]
12. Arushanov, E.; Lisunov, K.G. Transport properties of β-$FeSi_2$. *Jpn. J. Appl. Phys.* **2015**, *54*, 07JA02. [CrossRef]
13. Nozariasbmarz, A.; Agarwal, A.; Coutant, Z.A.; Hall, M.J.; Liu, J.; Liu, R.; Malhotra, A.; Norouzzadeh, P.; Öztürk, M.C.; Ramesh, V.P.; et al. Thermoelectric silicides: A review. *Jpn. J. Appl. Phys.* **2017**, *56*, 05DA04. [CrossRef]
14. Isoda, Y.; Udono, H. Preparation and Thermoelectric Properties of Iron Disilicide. In *Handbook of Thermoelectrics and Its Energy Harvesting, Preparation, and Characterization in Thermoelectrics*; Rowe, D.M., Ed.; CRC Press: Boca Raton, FL, USA; Taylor & Francis Group: Abingdon, UK, 2017; Chapter 18. [CrossRef]
15. Burkov, A.T. Silicide Thermoelectrics: Materials for Energy Harvesting. *Phys. Status Solidi A* **2018**, *215*, 1800105. [CrossRef]
16. Bahk, J.H.; Shakouri, A. Enhancing the thermoelectric figure of merit through the reduction of bipolar thermal conductivity with heterostructure barriers. *Appl. Phys. Lett.* **2014**, *105*, 052106. [CrossRef]
17. Gong, J.J.; Hong, A.J.; Shuai, J.; Li, L.; Yan, Z.B.; Ren, Z.F.; Liu, J.-M. Investigation of the bipolar effect in the thermoelectric material CaMg2Bi2 using a first-principles study. *Phys. Chem. Chem. Phys.* **2016**, *18*, 16566–16574. [CrossRef]
18. Chen, Z.W.; Zhang, X.; Ren, J.; Zeng, Z.; Chen, Y.; He, J.; Chen, L.; Pei, Y. Leveraging bipolar effect to enhance transverse thermoelectricity in semimetal Mg_2Pb for cryogenic heat pumping. *Nat. Commun.* **2021**, *12*, 3837. [CrossRef]
19. Du, X.L.; Qiu, P.F.; Chai, J.; Mao, T.; Hu, P.; Yang, J.; Sun, Y.Y.; Shi, X.; Chen, L.D. Doubled Thermoelectric Figure of Merit in p-Type β-$FeSi_2$ via Synergistically Optimizing Electrical and Thermal Transports. *ACS Appl. Mater. Interfaces* **2020**, *12*, 12901–12909. [CrossRef]
20. Sam, S.; Nakatsugawa, H.; Okamoto, Y. Optimization of Co additive amount to improve thermoelectric properties of β-$FeSi_2$. *Jpn. J. Appl. Phys.* **2022**, *61*, 111002. [CrossRef]
21. Ito, M.; Nagai, H.; Oda, E.; Katsuyama, S.; Majima, K. Effects of P doping on the thermoelectric properties of β-$FeSi_2$. *J. Appl. Phys.* **2002**, *91*, 2138. [CrossRef]
22. Tani, J.; Kido, H. Thermoelectric properties of Pt-doped β-$FeSi_2$. *J. Appl. Phys.* **2000**, *88*, 5810. [CrossRef]
23. Ohtaki, M.; Ogura, D.; Eguchi, K.; Arai, H. Thermoelectric Properties of Sintered $FeSi_2$ with Microstructural Modification. *Chem. Lett.* **1993**, *22*, 1067–1070. [CrossRef]
24. Chen, H.Y.; Zhao, X.B.; Stiewe, C.; Platzek, D.; Mueller, E. Microstructures and thermoelectric properties of Co-doped iron disilicides prepared by rapid solidification and hot pressing. *J. Alloys Compd.* **2007**, *433*, 338–344. [CrossRef]
25. Du, X.L.; Hu, P.; Mao, T.; Song, Q.F.; Qiu, P.F.; Shi, X.; Chen, L.D. Ru Alloying Induced Enhanced Thermoelectric Performance in $FeSi_2$-Based Compounds. *ACS Appl. Mater. Interfaces* **2019**, *11*, 32151–32158. [CrossRef] [PubMed]
26. Dabrowski, F.; Ciupinski, L.; Zdunek, J.; Krsuzewski, J.; Zybala, R.; Michalski, A.; Kurzydloski, J. Microstructure and thermoelectric properties of p and n type doped β-$FeSi_2$ fabricated by mechanical alloying and pulse plasma sintering. *Mater. Today-Proc.* **2019**, *8*, 531–539. [CrossRef]
27. Qiu, P.F.; Cheng, J.; Chai, J.; Du, X.L.; Xia, X.G.; Ming, C.; Zhu, C.X.; Yang, J.; Sun, Y.Y.; Xu, F.F.; et al. Exceptionally Heavy Doping Boosts the Performance of Iron Silicide for Refractory Thermoelectrics. *Adv. Energy Mater.* **2022**, *12*, 2200247. [CrossRef]
28. Komabayashi, M.; Hijikata, K.; Ido, S. Effects of Some Additives on Thermoelectric Properties of $FeSi_2$ Thin Films. *Jpn. J. Appl. Phys.* **1991**, *30*, 331–334. [CrossRef]
29. Nagai, H.; Maeda, I.; Katsuyama, S.; Majima, K. The Effects of Co and Ni Doping on the Thermoelectric Properties of Sintered β-$FeSi_2$. *J. Jpn. Soc. Powder Powder Metall.* **1994**, *41*, 560–564. [CrossRef]
30. Tani, J.; Kido, H. Electrical properties of Co-doped and Ni-doped β-$FeSi_2$. *J. Appl. Phys.* **1998**, *84*, 1408. [CrossRef]

31. Dąbrowski, F.; Ciupiński, Ł.; Zdunek, J.; Chromiński, W.; Kruszewski, M.; Zybała, R.; Michalski, A.; Kurzydłowski, K.J. Microstructure and Thermoelectric Properties of Doped $FeSi_2$ with Addition of B4C Nanoparticles. *Arch. Metall. Mater.* **2021**, *66*, 1157–1162. [CrossRef]

32. Qu, X.; Lü, S.; Hu, J.; Meng, Q. Microstructure and thermoelectric properties of β-$FeSi_2$ ceramics fabricated by hot-pressing and spark plasma sintering. *J. Alloys Compd.* **2011**, *509*, 10217–10221. [CrossRef]

33. Nogi, K.; Kita, T. Rapid production of β-$FeSi_2$ by spark-plasma sintering. *J. Mater. Sci.* **2000**, *35*, 5845–5849. [CrossRef]

34. Dezsi, I.; Fetzer, C.; Kiss, M.; Degroote, S.; Vantomme, A. Site location of Co in β-$FeSi_2$. *J. Appl. Phys.* **2005**, *98*, 073523. [CrossRef]

35. Takeuchi, T. New Thermoelectric Materials with Precisely Determined Electronic Structure and Phonon Dispersion. In *Handbook of Thermoelectrics and Its Energy Harvesting, Preparation, and Characterization in Thermoelectrics*; Rowe, D.M., Ed.; CRC Press: Boca Raton, FL, USA; Taylor & Francis Group: Abingdon, UK, 2017; Chapter 7.

36. Kojima, T.; Masumoto, K.; Okamoto, M.A.; Nishida, I. Formation of β-$FeSi_2$ from the sintered eutectic alloy $FeSi$-Fe_2Si_5 doped with cobalt. *J. Less Common Met.* **1990**, *159*, 299–305. [CrossRef]

37. Mott, N.F. Conduction in glasses containing transition metal ions. *J. Non-Cryst. Solids* **1968**, *1*, 1–17. [CrossRef]

38. Zhang, Q.; Liao, B.L.; Lan, Y.C.; Lukas, K.; Liu, W.S.; Esfarjani, K.; Opeil, C.; Broido, D.; Chen, G.; Ren, Z.F. High thermoelectric performance by resonant dopant indium in nanostructured SnTe. *Proc. Natl. Acad. Sci. USA* **2013**, *110*, 13261–13266. [CrossRef]

39. Zhao, L.D.; Lo, S.H.; He, J.Q.; Li, H.; Biwas, K.; Androulakis, J.; Wu, C.I.; Hogan, T.P.; Chung, D.Y.; Dravid, V.P.; et al. High Performance Thermoelectrics from Earth-Abundant Materials: Enhanced Figure of Merit in PbS by Second Phase Nanostructures. *ACS J. Am. Chem. Soc.* **2011**, *133*, 20476–20487. [CrossRef]